China's First Infrared Occultation Spectrometer (GaoFen-5/AIUS) Monitoring Atmosphere Above Antarctic: Evaluation of Methane Profiles

Shuanghui Liu, Xiaoying Li, Jian Xu, *Senior Member, IEEE*, Hailiang Shi, Yuhang Guo, Xingying Zhang, Shule Ge, Yapeng Wang, Hongmei Wang, Xifeng Cao, Lanlan Rao, and Jiancheng Shi, *Fellow, IEEE*

***Abstract*—The atmospheric infrared ultraspectral sounder (AIUS) is China's first infrared occultation spectrometer onboard the GaoFen-5 satellite. This instrument provides measurements in the near-infrared and mid-infrared spectral regions with a spectral resolution of 0.02 cm^{-1}, monitoring key greenhouse gases like methane (CH_4). In this study, we have developed a physics-based retrieval algorithm for accurately deriving CH_4 mole fraction profiles from infrared absorption spectra. The retrieval algorithm is applied to the AIUS and successfully obtains CH_4 mole fraction profiles from January to December 2019 over Antarctic. The validation results show that the retrieval algorithm has a satisfactory performance using AIUS measurements, with average relative standard deviation of the differences less than 7.2% throughout the altitude range of 10–70 km.**

***Index Terms*—Antarctic, GaoFen-5 (GF-5)/atmospheric infrared ultraspectral sounder (AIUS), methane (CH_4), retrieval algorithm.**

I. Introduction

METHANE (CH_4) is a chemically and radiatively active gas in the atmosphere and is the second most important anthropogenic greenhouse gas after carbon dioxide (CO_2) [1]. Before the 1970s, scientists measured atmospheric CH_4 concentrations by analyzing air trapped in polar ice cores. Direct measurements of CH_4 in the troposphere began in 1978 [2], [3]. Currently, CH_4 concentrations can be obtained through discrete air samples collected at the ground surface, as well as through remotely sensed measurements of atmospheric CH_4 columns obtained from the ground surface or space. According to data from the National Oceanic and Atmospheric Administration, the global annual concentration of CH_4 has been constantly changing since 1983. These data indicate a sustained increase in atmospheric CH_4 concentrations in the 1980s, a stable period between 1999 and 2005, and generally rapid growth after 2005. In 2022, the concentration of CH_4 reached 1911.83 $\pm$ 0.59 ppb [4].

Compared to traditional methods based on ground-based observations or air sampling, satellite measurements have several advantages, including stability, continuity, large-scale coverage, and convenient access to globally spatiotemporal distribution. Satellite remote sensing has become a major tool over the past decades for monitoring greenhouse gases, such as CH_4 and CO_2. In 1979, the stratospheric and mesospheric sounder on the Nimbus-7 satellite measured the global distribution of stratospheric CH_4 concentration for the first time [5]. Afterward, several satellite sensors have been launched to measure the vertical column densities and concentration profiles of CH_4. The CH_4 column densities can be retrieved from near-infrared radiance measured by instruments, such as the scanning imaging absorption spectrometer for atmospheric chartography [6] and the tropospheric monitoring instrument [7]. The instruments, such as the Michelson interferometer for passive atmospheric sounding [8], the atmospheric infrared sounder [9], the atmospheric chemistry experiment—Fourier transform spectrometer (ACE-FTS) [10], and the tropospheric emission sounder [11] can observe CH_4 profiles based on thermal infrared emission. The thermal and near-infrared sensor for Carbon Observation Fourier Transform Spectrometer-2 [12] can retrieve the CH_4 columns and profiles from SWIR spectra and TIR spectra, respectively [13].

GaoFen-5 (GF-5) is a high-resolution remote sensing satellite that was launched on May 9, 2018 (Beijing local time). The satellite was designed to fly in a high-inclination (98.2°) circular low-Earth orbit, located 705 km above the Earth's surface, with

Manuscript received 30 October 2023; revised 23 January 2024 and 25 February 2024; accepted 21 March 2024. Date of publication 27 March 2024; date of current version 12 April 2024. This work was supported in part by the Chinese Academy of Sciences (CAS) "Pioneering Initiative Talents Program" under Grant E1RC2WB2, in part by the National Key Research and Development Program of China under Grant 2022YFF0606404, and in part by Basic Strengthening Program Technical Field Foundation under Grant 2023KJC-Y-0193. *(Corresponding authors: Xiaoying Li; Jian Xu.)*

Shuanghui Liu, Jian Xu, Lanlan Rao, and Jiancheng Shi are with the National Space Science Center, Chinese Academy of Sciences, Beijing 100190, China (e-mail: liushuanghui@nssc.ac.cn; xujian@nssc.ac.cn; raolanlan@nssc.ac.cn; shijc@radi.ac.cn).

Xiaoying Li is with the Aerospace Information Research Institute, Chinese Academy of Sciences, Beijing 100094, China, and also with the Innovation Center for FengYun Meteorological Satellite (FYSIC), Beijing 100081, China (e-mail: lixy01@radi.ac.cn).

Hailiang Shi is with the Anhui Institute of Optics and Fine Mechanics, Chinese Academy of Sciences, Hefei 230031, China (e-mail: hlshi@aiofm.ac.cn).

Yuhang Guo is with the Aerospace Information Research Institute, Chinese Academy of Sciences, Beijing 100094, China (e-mail: guoyuhang21@mails.ucas.ac.cn).

Xingying Zhang, Yapeng Wang, and Xifeng Cao are with the National Satellite Meteorological Center, China Meteorological Administration, Beijing 100081, China (e-mail: zxy@cma.gov.cn; wangyp@cma.gov.cn; caoxifeng18@mails.ucas.ac.cn).

Shule Ge is with the China Center for Resources Satellite Data and Application, Beijing 100094, China (e-mail: gslcresda@126.com).

Hongmei Wang is with Nantong University, Nantong 226019, China (e-mail: wanghongmei@ntu.edu.cn).

Digital Object Identifier 10.1109/JSTARS.2024.3381651

© 2024 The Authors. This work is licensed under a Creative Commons Attribution-NonCommercial-NoDerivatives 4.0 License. For more information, see https://creativecommons.org/licenses/by-nc-nd/4.0/

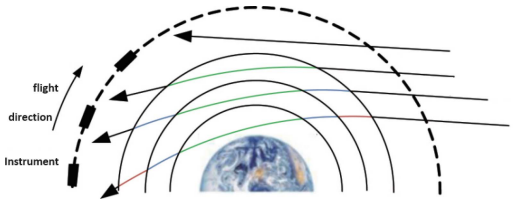

Fig. 1. Illustration of the AIUS solar occultation observation [24].

the local time of ascending node at 13:00 [14]. GF-5 is equipped with six payloads designed to achieve various scientific objectives and has a projected lifespan of eight years [15]. However, the GaoFen-5 satellite lost contact with the ground station and has been out of service since April 2020. The atmospheric infrared ultraspectral sounder (AIUS) on board the GF-5 satellite, designed by the Beijing Institute of Space Mechanics and Electricity, is China's first solar occultation infrared spectrometer. The AIUS was designed to detect O_3 and other atmospheric compositions related to ozone depletion, with a specific focus on the atmosphere above Antarctic [16], [17]. The main scientific objectives of the AIUS are to provide high-precision observations for atmospheric environmental monitoring and climate change research, and to promote the development of China's occultation/limb measurement technology [17].

Presently, only a few studies on AIUS trace gas retrievals have been conducted. Wang et al. [18] used simulated spectra to retrieve the profiles of N_2O, NO_2, and HF in order to validate the suitability of the OEM algorithm using the parameters of GF-5 AIUS. Cao et al. [19] applied a channel selection algorithm to the AIUS and retrieved temperature profiles from the AIUS. Li et al. [16], [20] evaluated the obtained AIUS Level-1 data and performed the first retrievals of O_3, H_2O, and HCl profiles from AIUS spectra. CH_4 is an important greenhouse gas and its spatiotemporal variations over Antarctic strongly associate with global warming and climate change.

In addition to the AIUS, the ACE-FTS is the only instrument that is currently available for measuring CH_4 profiles over Antarctic. The AIUS is similar to the ACE-FTS in terms of observation geometry and can serve as a complement to the ACE-FTS. It is an important data source for monitoring CH_4 in polar regions.

Currently, the AIUS have demonstrated its potential for retrieving O_3, H_2O, HCl, and other gases. Considering the role of CH_4 in global warming and climate change [21], [22], the vertical distribution of CH_4 over Antarctic has not yet been adequately observed. Therefore, this article focuses on the AIUS CH_4 inversion. Here, we develop a retrieval algorithm based on the radiative transfer calculations and optimal estimation for deriving CH_4 profiles from AIUS spectra during the whole year of 2019 and analysis the spatiotemporal variations over Antarctic. This study will, for the first time, focus on retrieving CH_4 profiles using AIUS measurements and expand the application scope of the first domestic infrared occultation satellite.

The rest of this article is organized as follows. In Section II, the measurements and methodology are introduced, followed by a brief description of the AIUS instrument and Level-1 data, the retrieval method, and the channel selection. The results of AIUS CH_4 retrieval over the Antarctic, the error analysis, and the comparison with the ACE-FTS CH_4 data are discussed in Section III. Finally, Section IV concludes this article.

II. Measurements and Methodology

A. Overview of the AIUS Instrument and Level-1 Data

During sunrise in orbit, the AIUS measured the solar transmittance spectrum of the tangential atmosphere from the horizon to the outer atmosphere (as shown in Fig. 1) within a bandwidth of 750 to 4100 cm $^{-1}$ along the altitude from 8 to 100 km. It carried out this measurement with a high spectral resolution of 0.02 cm^{-1}. The pressure, temperature, and concentrations of atmospheric species (such as O_3, H_2O, HCl, NO_2, N_2O, HF, etc.) were retrieved from the specific spectral absorption lines of different atmospheric components. Its latitudinal coverage ranged from 55 °S to 90 °S.

The AIUS was implemented with two types of photovoltaic detectors: Mercury Cadmium Telluride (MCT) and Indium Antimonide (InSb). The spectral calibration precision met the requirements for atmospheric trace gas inversion [23]. Their spectral ranges were 750—1850 cm^{-1} and 1850–4100 cm^{-1}, respectively. The AIUS utilized ultraresolution Fourier transform spectrometer technology and sun-tracking system technology to provide observations with a high spectral resolution [24].

Converting the AIUS Level-0 data (raw measurements) to Level-1 data (irradiance spectra) required a series of processing and calibration steps, including data preparation, interferogram reconstruction, spectrum computation, spectral calibration, and transmittance calculation [16], [24].

The first step was to acquire and process the auxiliary data. The Level-0 data consisted of interferometric measurements downloaded from the spacecraft, along with the acquisition time, sun position, and satellite position. These parameters were used to calculate the geometric parameters, altitude, and geographic location (latitude and longitude).

The AIUS operated in low Earth orbit. The interferogram experienced spikes due to the influence of charged particles. The second step was to calculate the interference values at the spikes in order to reconstruct the interferogram using interpolation or statistical methods.

In the third step, the fast Fourier transform was used to calculate the spectrum from the reconstructed interferogram. Accurate calibration is an essential technology for obtaining precise measurements of O_3, CO_2, and CH_4 concentrations. The fourth step involved spectral calibration, which included correcting for Doppler shift, selecting suitable lines, and accurately determining peak positions [24].

The final step was to calculate the transmittance. The Level-1 data product includes transmittance, instrument line shape (ILS), as shown in Fig. 2, as well as observation geometry and other processed auxiliary data. The relationship between transmittance and the digital number is shown as follows [16]:

$$\tau(h,\lambda) = \frac{D(h,\lambda) - B(h,\lambda)}{S(h,\lambda) - B(h,\lambda)} \quad (1)$$

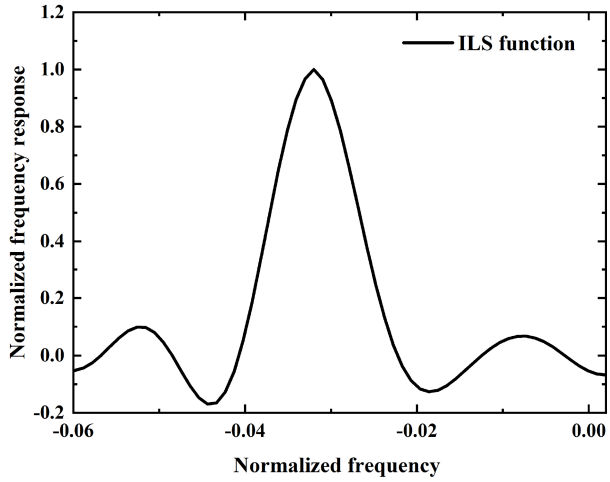

Fig. 2. ILS function of the AIUS.

where h represents the tangent; λ denotes the wavenumber; and $D(h,\lambda)$, $B(h,\lambda)$, and $S(h,\lambda)$ refer to the digital number value, the deep space signal, and the solar radiation outside the atmosphere, respectively.

B. Retrieval Method

The retrieval method comprises a forward model based on the reference forward model (RFM) and an inversion procedure based on the optimal estimation method (OEM). Ignoring scattering and assuming local thermodynamic equilibrium, the radiative transfer equation for the radiation intensity at wavenumber v received by an instrument at position s is as follows [25], [26]:

$$I(v,s) = I(v,s_0)e^{-\tau(v;s_0,s)} + \int_{s_0}^{s} B(v,T(s'))e^{-\tau(v;s',s)}\alpha(v,s')ds' \quad (2)$$

where $I(v,s_0)$ represents the background contribution at wavenumber v and position s_0, τ denotes the optical depth, $B(v,T)$ signifies the radiance emitted by a black body at temperature T, and $\alpha(v,s')$ represents the volume absorption coefficient from position s_0 to position s. On the right side of (2), the first term represents the attenuated radiation, while the second term represents the increase in radiance caused by atmospheric thermal emission. In this equation, $B(v,T)$ is represented by the Planck function, shown as follows:

$$B(v,T) = \frac{2hc^2v^3}{e^{hcv/k_BT}-1} \quad (3)$$

where h represents the Planck constant and k_B denotes the Boltzmann constant, respectively. The transmittance calculated by the radiation transfer model is shown as follows [27]:

$$\begin{aligned}\tau &= e^{-\sum \chi} \\ &= e^{-\sum k\mu} \\ &= e^{-\sum k_{(v,p,T,e)} \int v\rho ds}\end{aligned} \quad (4)$$

where χ is the optical thickness, k is the absorption coefficient, which is in general a function of the wavenumber v, pressure p, temperature T, and partial pressure e. μ is the absorber amount, which is related to the volume mixing ratio (VMR) of the absorber $\boldsymbol{v}$, the (molecular) air density ρ, and the distance along the path s.

We typically used a discrete version of the nonlinear data model for the radiative transfer equation. Equation (2) can be replaced with

$$\boldsymbol{y} = \boldsymbol{F}(\boldsymbol{x},\boldsymbol{b}) + \boldsymbol{\epsilon} \quad (5)$$

where $\boldsymbol{y}$ represents the measurement vector, which refers to the measurement of transmittance [see (1)]; and $\boldsymbol{F}$ denotes the radiative transfer model, which represents the simulated transmittance [see (4)]. In this study, the RFM [27], [28] is used for line-by-line radiative transfer calculations. $\boldsymbol{x}$ refers to the state vector; $\boldsymbol{b}$ represents the forward model parameters; and $\boldsymbol{\epsilon}$ denotes the vector of measurement noise.

The retrieval method utilizes the OEM to find a solution estimate that minimizes a cost function, which can be written as [29]

$$\begin{aligned}\boldsymbol{\chi^2} = &(\boldsymbol{y}-\mathbf{F}(\mathbf{x},\mathbf{b}))^T\mathbf{S}_\epsilon^{-1}(\boldsymbol{y}-\mathbf{F}(\mathbf{x},\mathbf{b})) \\ &+ (\boldsymbol{x}-\boldsymbol{x_a})^T\mathbf{S_a^{-1}}(\boldsymbol{x}-\boldsymbol{x_a})\end{aligned} \quad (6)$$

where $\mathbf{x}_a$ represents a priori profile, $\mathbf{S}_a$ denotes a priori covariance matrix, $E|(\boldsymbol{x}-\boldsymbol{x_a})(\boldsymbol{x}-\boldsymbol{x_a})^T|$, $\mathbf{S}_\epsilon$ signifies the covariance matrix for measurement errors, $\mathbf{KS_aK}^T$, and $\mathbf{K}$ represents the Jacobian matrix, $\frac{\partial F(\boldsymbol{x})}{\partial \boldsymbol{x}}$.

Newtonian iteration is a straightforward numerical technique to find the root of the gradient of (6) when the problem is not highly nonlinear. For the general vector equation, $\boldsymbol{g}(\boldsymbol{x}) = 0$. The function $\boldsymbol{g}(\boldsymbol{x})$ is the derivative of the cost function (6) and $\nabla_x \boldsymbol{g}$ is the second derivative. The iteration is similar to Newton's method for the scalar case and can be expressed as

$$\boldsymbol{x_{i+1}} = \boldsymbol{x_i} - [\nabla_x \boldsymbol{g}(\boldsymbol{x_i})]^{-1}\boldsymbol{g}(\boldsymbol{x_i}). \quad (7)$$

Calculate $\boldsymbol{g}(\boldsymbol{x})$ and $\nabla_x \boldsymbol{g}$ based on (6), and substitute into the Newtonian iteration (7). In the Gauss–Newton method, the next iteration is given by

$$\begin{aligned}\boldsymbol{x}_{i+1} = \boldsymbol{x}_i + &\left(\mathbf{S}_a^{-1} + \mathbf{K}_i^T\mathbf{S}_\epsilon^{-1}\mathbf{K}_i\right)^{-1} \\ &\left(\mathbf{K}_i^T\mathbf{S}_\epsilon^{-1}\left(\boldsymbol{y}-\boldsymbol{F}(\boldsymbol{x}_i)\right) - \mathbf{S}_a^{-1}\left(\boldsymbol{x}_i-\boldsymbol{x}_a\right)\right).\end{aligned} \quad (8)$$

When the true solution is significantly far from the current iteration point, the Newton iteration will be invalid. In the retrieval of O_3, H_2O, and HCl profiles from AIUS measurements, Li et al. [16] used the Levenberg–Marquardt (LM) method to solve the underlying least-squares fitting problem. In the LM method, the cost function is minimized by introducing a constraint factor, denoted as γ. A new iterate is as follows:

$$\begin{aligned}\boldsymbol{x}_{i+1} = \boldsymbol{x}_i + &\left((1+\gamma)\,\mathbf{S}_a^{-1} + \mathbf{K}_i^T\mathbf{S}_\epsilon^{-1}\mathbf{K}_i\right)^{-1} \\ &\left(\mathbf{K}_i^T\mathbf{S}_\epsilon^{-1}\left(\boldsymbol{y}-\boldsymbol{F}(\boldsymbol{x}_i)\right) - \mathbf{S}_a^{-1}\left(\boldsymbol{x}_i-\boldsymbol{x}_a\right)\right)\end{aligned} \quad (9)$$

where γ represents a smoothing factor. When $\gamma \to 0$, (8) and (9) are similar. For more details on the retrieval procedure, refer to [16], [29], [30], [31], [32], [33].

TABLE I
MODEL PARAMETERS AND EXTERNAL DATA SOURCES

Atmospheric parameters	**Description**
Temperature profile	MLS retrievals
Pressure profile	MLS retrievals
Interfering species	MLS, ACE-FTS and AFGL
CH_4	Li et al. [16]
Spectroscopic parameters	**Description**
Spectroscopic data	HITRAN2016
Instrument parameters	**Description**
Viewing geometry	Occultation
Tangent Height	the tangent height of AIUS
Instrument line shape	see Fig. 2
Field of view	1.25 mrad
Observer Altitude	705 KM

The error analysis is essential for retrieving the atmospheric composition. There are three types of errors that can be characterized by their respective error covariance: the covariance of the smoothing error ($\mathbf{S}_s$), the covariance of the forward model error ($\mathbf{S}_p$, which includes spectroscopy, temperature, and pressure error), and the covariance of the retrieval random noise error ($\mathbf{S}_m$) [29], given as follows:

$$\mathbf{S}_s = (\mathbf{A}-\mathbf{I})\mathbf{S}_a(\mathbf{A}-\mathbf{I})^T \tag{10}$$

$$\mathbf{S}_p = \mathbf{G}\mathbf{K}_b\mathbf{S}_b\mathbf{K}_b^T\mathbf{G}^T \tag{11}$$

$$\mathbf{S}_m = \mathbf{G}\mathbf{S}_\epsilon\mathbf{G}^T \tag{12}$$

$$\boldsymbol{e} = \sqrt{\mathbf{S_s}+\mathbf{S_p}+\mathbf{S_m}} \tag{13}$$

where $\mathbf{A}$ represents the Averaging Kernel (AK) matrix, $\mathbf{A} = \mathbf{G}\mathbf{K}$; $\mathbf{I}$ denotes the identity matrix; $\mathbf{G}$ refers to the gain matrix, $\mathbf{G} = (\mathbf{K}^T\mathbf{S}_\epsilon^{-1}\mathbf{K} + \mathbf{S_a^{-1}})^{-1}\mathbf{K^T}\mathbf{S}_\epsilon^{-1}$; $\mathbf{S}_b$ represents the error covariance matrix of b; and $\mathbf{K}_b$ denotes the Jacobian matrix with respect to the parameters of the forward model. The calculation of matrices $\mathbf{G}$ and $\mathbf{A}$ is realized by coding, whereas $\mathbf{K}$ is obtained from the forward model. The smoothing error ($\boldsymbol{e_s}$), the forward model error ($\boldsymbol{e_p}$), and the retrieval random noise error ($\boldsymbol{e_m}$) can be represented by the square roots of $\boldsymbol{S_s}$, $\boldsymbol{S_p}$, and $\boldsymbol{S_m}$, respectively. The total error ($\boldsymbol{e}$), is calculated as the square root of the sum of the aforementioned covariance.

The parameters in the forward model include the CH_4 retrieval channel, spectral resolution, the absorbing species, atmospheric profiles, viewing geometry, spectroscopic data, ILS, and the field of view [27] (see Table I). Within the wavelength range used in this experiment, there are no significant differences between the CH_4 versions of HITRAN 2020 and HITRAN 2016. The spectroscopic parameters for CH_4, N_2O, H_2O, and other species were taken from the HITRAN 2016 database [34].

The interfering species profiles were constructed using atmospheric models from the Air Force Geophysics Laboratory, Microwave Limb Sounder (MLS) Level-2 products, and the ACE-FTS Climatology Version 4.1. The atmospheric profiles cover the altitude range from 0 to 102 km with a vertical grid of 1, 2, and 3 km in the ranges of 0–50 km, 50–90 km, and above 90 km, respectively. The a priori information for the CH_4 VMR was constructed following the methodology outlined by Li et al. [16].

C. Channel Selection

The AIUS has 167 501 spectral bands that contain a significant amount of information but cannot be directly used for CH_4 retrieval. High spectral resolution measurements allow for the separation of individual bands. We use microwindows to enhance computational efficiency and reduce errors caused by interfering species [35].

First, we analyzed the absorption of atmospheric molecules in the 750–4100 cm^{-1} range using data on the atmospheric molecular absorption spectrum from the HITRAN website.[1] Combining the four spectral features with the significant absorption points of CH_4 in the infrared spectrum (2913 cm^{-1}, 1533.3 cm^{-1}, 3018.9 cm^{-1}, and 1305.9 cm^{-1}) and considering the absorption of interfering components, we initially screened three broad spectral absorption ranges: 1130–1660 cm^{-1}, 2470–3160 cm^{-1}, and 3820–3910 cm^{-1}. And then, based on the absorption windows of potential interfering components in the radiative transfer model (refer to Table II), we selected seven initial inversion spectral windows for CH_4, namely 1200–1230 cm^{-1}, 1330–1340 cm^{-1}, 1380–1500 cm^{-1}, 1550–1660 cm^{-1}, 2645–2980 cm^{-1}, 3820–3822 cm^{-1}, and 3865–3920 cm^{-1}. These windows were selected to minimize interference from other atmospheric species.

The seven aforementioned microwindows still contain 33 107 spectral bands. Using these bands for retrieval is still inefficient in terms of data management and computational resources. Finally, We selected the retrieved channels based on the measure of information entropy. The channel selection method mainly includes the following four main stages.

Step 1: Calculate the background error covariance matrix ($\mathbf{S}_a$).

Step 2: Calculate the observed covariance matrix ($\hat{\mathbf{S}}$). The observation covariance matrix can be written as [36]

$$\hat{\mathbf{S}} = \mathbf{S}_a - \mathbf{S}_a\mathbf{K}^T(\mathbf{K}\mathbf{S}_a\mathbf{K}^T + \mathbf{S}_\epsilon)^{-1}\mathbf{K}\mathbf{S}_a. \tag{14}$$

The third step is to calculate the information capacity ($\mathbf{H}$). If $\mathbf{S}_a$ and $\hat{\mathbf{S}}$ are known, the information capacity included in the observation process is recorded as follows:

$$\mathbf{H} = \frac{\ln|\mathbf{S}_a| - \ln|\hat{\mathbf{S}}|}{2}. \tag{15}$$

The final step is to obtain the channels through iterative processes. At each iteration, only the channel with the highest value of H is selected.

After conducting an analysis on disturbance in atmospheric components and performing experiments to channel selection, we were able to obtain 120 spectral bands for CH_4 retrieval. These bands are shown in Fig. 3. On most CH_4 microwindows, the spectra were of high quality with a signal-to-noise ratio (SNR) of 200–350 [16].

We compared the AIUS CH_4 retrieval bands used in this experiment with the officially announced ACE-FTS CH_4 retrieval bands, as shown in Fig. 3. The gray line represents the simulated transmittance, while the blue dot denotes the ACE-FTS

[1][Online]. Available: https://hitran.org/

TABLE II
FITTING WINDOWS

atmospheric parameter	sensitivity wavelength (cm^{-1})		
Temperature	1300, 1525	-	3850
Pressure	1250 – 1300	3000 – 3100	-
CO_2	1230 – 1270, 1340 – 1380	2480 – 2530, 2580 – 2645	3830
H_2O	1500 – 1550	2980 – 3160	-
N_2O	1140 – 1200, 1240 – 1330	2470 – 2490, 2525 – 2600	3822 – 3835,3840 – 3860
O_3	1130 – 1170	3000 – 3060	3825 – 3850, 3855 – 3865

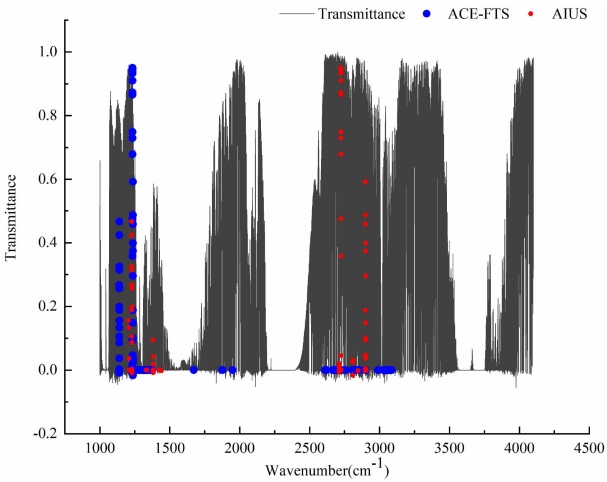

Fig. 3. Comparison of the AIUS and ACE-FTS CH_4 retrieval channels.

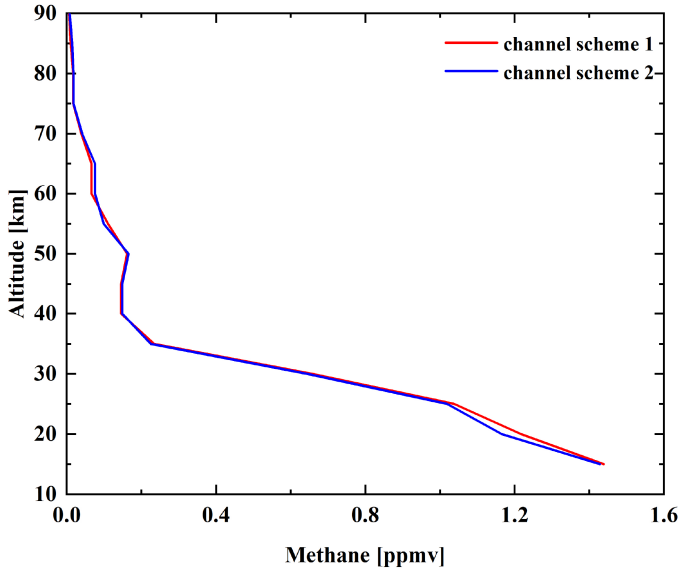

Fig. 4. CH_4 profiles were retrieved from two different channel schemes. The retrieval was carried for AIUS measurements recorded on May 16, 2019. The red line represents the CH_4 profile retrieved from the 120 channels, while the blue line refers to the CH_4 profile retrieved from 1115 channels.

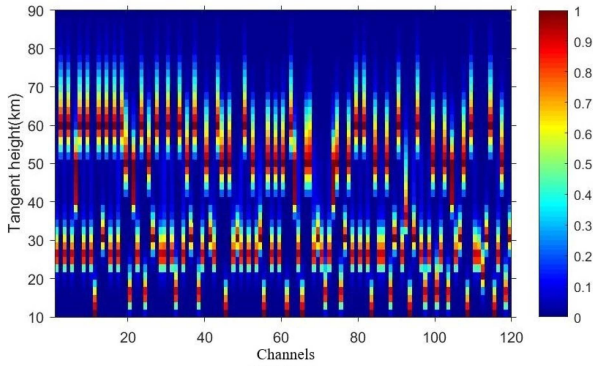

Fig. 5. Weight function matrix of AIUS channels.

CH_4 retrieval bands, and the red dot indicates the AIUS CH_4 retrieval bands. The CH_4 channel selection results from this experiment are primarily included in the ACE-FTS CH_4 inversion channel, except for the spectral range of 1500–2000 cm^{-1}. ACE-FTS CH_4 experiments use a spectral range spanning from 1500 to 2000 cm^{-1} to enhance CH_4 retrieval. However, in our experiment, we excluded this microwindow to eliminate H_2O interference on the retrieval performance.

CH_4 retrieval experiments were conducted using two different channel schemes, as illustrated in Fig. 4. The CH_4 concentration profiles retrieved using two different channel schemes show a similar variation trend with height, but the retrieval efficiency of the AIUS retrieval scheme 1 (using 120 channels) is 24 times higher than that of the channel scheme 2 (using 1115 channels).

Fig. 5 illustrates the weight function values of the 120 selected channels in the order of their selection. The horizontal axis represents the selected channels, the vertical axis represents the tangent height, and the color bar represents the weight. The 120 selected channels covered the altitude range from the troposphere to the mesosphere, and the tangent heights at which the extreme values of each channel weight function varied sequentially.

III. RESULTS AND DISCUSSION

A. AIUS CH_4 Retrievals

Unfortunately, the AIUS instrument has been out of service since April 2020. The spectral measurements after 2019 were lost due to malfunctions at the ground station. To obtain a more solid outcome, we have included Level-1 data from the commissioning phase (from January to March 2019) for additional retrieval experiments. In this study, we used 246 orbits of AIUS spectra observed in different months for retrieval. Table III presents the temporal and spatial characteristics of the AIUS data we used in this experiment, which were categorized into five latitude zones: 60–65°S, 65–70°S, 70–75°S, 75–80°S, and 80–85°S.

The value of the averaging kernel (AK) represents the contribution of the measurement data in the retrieval. The AK shape describes the vertical resolution of the retrieved profile [37]. The

TABLE III
INFORMATION ON THE AIUS DATA USED IN THIS RESEARCH

Latitude Zone	Month
60 – 65°S	Jan, Nov, Dec
65 – 70°S	Jan, May, Jun, Jul, Nov
70 – 75°S	Feb, May, Aug
75 – 80°S	Feb, Apr, Aug, Oct
80 – 85°S	Mar, Apr, Sep, Oct

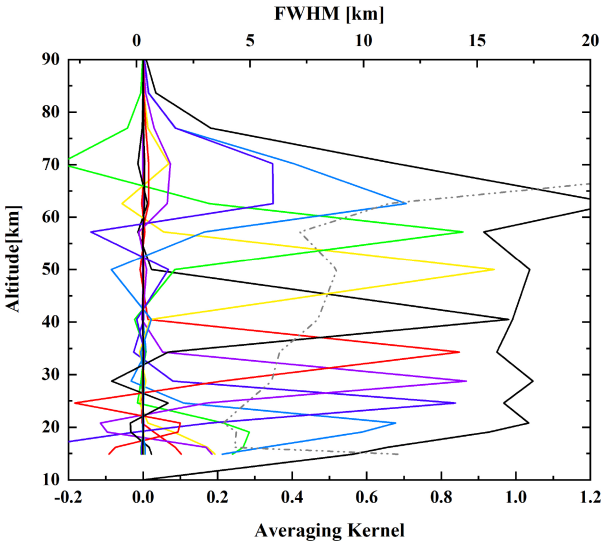

Fig. 6. Averaging kernel of a single CH_4 profile. The retrieval was carried for AIUS measurements recorded on May 16, 2019. The colorful solid line represents the averaging kernel, while the gray line indicates the FWHM. The black solid line expresses the sum of the average kernel at each altitude.

AK and the full-width-at-half-maximum (FWHM) of AIUS data on May 16, 2019 are shown in Fig. 6. When the altitude is below 15 km or above 65 km, the AK value is less than 0.3. When the altitude is between 15 and 65 km, the AK value falls within the range of 0.7–1. It indicates that the information on CH_4 retrieval mainly comes from the AIUS measurement data in this experiment. The FWHM reaches 4–11 km across the altitude range from 10 to 65 km. Above 65 km, the FWHM exceeds 20 km.

The residuals between the measured spectra and the simulated spectra are shown in Fig. 7. The spectral residuals between the simulated and measured spectra are within $\pm$ 0.2 and $\pm$ 0.03 at the tangent heights of 40.5 and 70.2 km, respectively. This indicates that the residual transmittance of the measured data is lower at the higher tangent height compared to the simulated spectra.

We calculated the monthly average value of the CH_4 profiles, as shown in Fig. 8. It illustrates that CH_4 concentrations show significant seasonal variations over Antarctic. In each season, the monthly mean CH_4 profile is similar during consecutive months, such as April–May, July–August, and November–December.

The monthly average VMR in November and December is higher than that in other months for altitudes ranging from 21 to 76 km. These two months are the warm season in Antarctica, during which there may be an increase in the release of CH_4 from ocean sediment and permafrost. This can result in an increase in the CH_4 VMR in the atmosphere [38]. The average VMR in

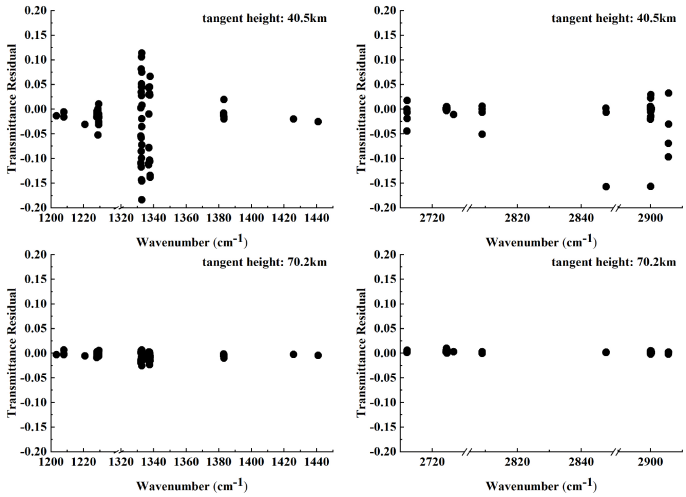

Fig. 7. Comparison of residual transmittance between measured and simulated spectra. The AIUS measurements were recorded on May 16, 2019. Four spectra are plotted for tangent heights at 40.5 and 70.2 km, respectively.

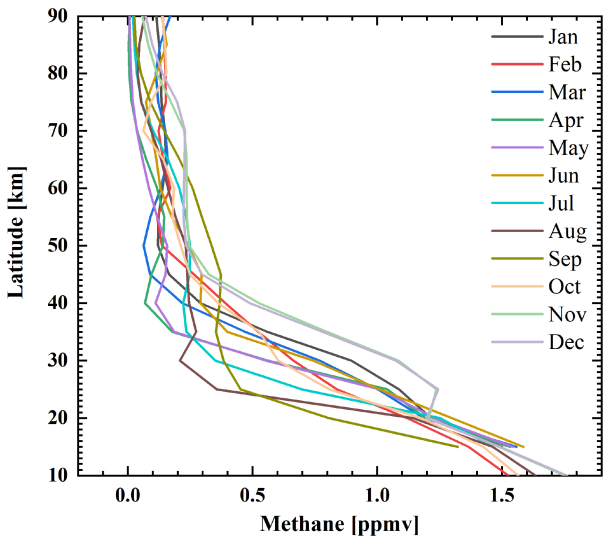

Fig. 8. Comparison of the AIUS CH_4 profiles in different months.

April and May is lower than in other months for altitudes above 57 km. Below 57 km, as altitude increases, the monthly average VMRs in September, August, April, and March are lower than those in other months. The VMR value of CH_4 decreases as altitude increases. The CH_4 VMR is approximately 1.17–1.65 ppmv between 10 and 20 km, and decreases to less than 0.2 ppmv at 35 km in April and May.

Due to the characteristics of AIUS measurements, it is impossible to observe the same latitude zone every month, and we cannot obtain measurement data for the same latitude zone each month. The aforementioned analysis results may be influenced by latitude. So, we also analyzed the average CH_4 profiles in different latitude zones, as shown in Fig. 9.

Fig. 9 illustrates that CH_4 concentrations show significant latitude variations over Antarctica. The average VMR in 60 – 65° S is higher than that in other months, ranging from 21 to 90 km. The VMR of CH_4 decreases with increasing altitude.

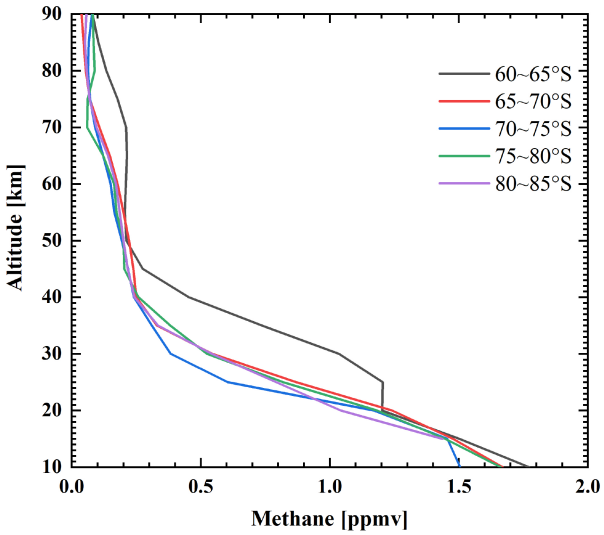

Fig. 9. Comparison of the AIUS CH_4 profiles in different latitude zones.

TABLE IV
MODEL PARAMETER ERRORS CONSIDERED IN THE AIUS CH_4 RETRIEVALS.

Atmospheric parameters	Perturbation
Temperature	1K
Pressure	1%
Line strength	
CH_4	4%
H_2O	1%
CO_2	5%
N_2O	1%
O_3	1%

As can be seen from Figs. 8 and 9, certain profiles lack numerical values at the 10-km mark. The tangent height measured by the AIUS is sometimes higher than 10 km, which makes it impossible to retrieve the CH_4 concentration at this altitude.

B. Error Characterization

In the retrieval experiment, it is necessary to assess the uncertainties of atmospheric parameters, such as temperature and pressure, among others, that are used in the experiment. In this study, we consider the potential sources of error, including smoothing error, forward model error, and random noise error. The sources of error, and the corresponding perturbation amounts are shown in the Table IV.

The precision of the MLS version 4 temperature and pressure measurements is better than 1 K and 1% from the upper troposphere to the stratosphere [39], [40], [41], respectively. In this study, we found errors caused by the uncertainties in temperature and pressure to be 4.82E-04 ppmv (0.15%), and 2.70E-03 ppmv (0.44%), respectively.

The CH_4 intensities in HITRAN 2016 [34] are derived from the HITRAN 2012 and the MeCaSDa database below 1370 cm^{-1}, and they remain unchanged from the HITRAN 2012 intensities in the 1370–4000 cm^{-1} region. The uncertainty of CH_4 line intensities used in this experiment is smaller than 4% [42], [43], [44], which can cause a bias of 6.17E-03 ppmv (1.27%). The uncertainty of H_2O and CO_2 line intensity is 1% and 5% [45], respectively. Unfortunately, we did not find official information on the uncertainty of N_2O and O_3 line strength within the AIUS CH_4 retrieval channels; we have chosen to apply a 1% perturbation as a conservative estimate of the actual uncertainty. The uncertainties in line intensity of the four atmospheric components mentioned previously (H_2O, CO_2, N_2O, and O_3) contribute to a deviation of 1.38E-05 ppmv (1.90E-03%).

Individual estimates of various errors and relative errors for the CH_4 retrieval are shown in Fig. 10. Below 25 km, the total error is mainly attributed to random noise and smoothing error, while above 25 km, the total error is primarily due to spectroscopy and random noise error. The uncertainties in temperature and pressure have a relatively minor impact on the total error.

C. Validation Using ACE-FTS Observations

The ACE-FTS is a solar occultation measurement instrument on board SCISAT-1, which was launched in August 2003. The satellite is in a circular orbit at an altitude of 650 km and an inclination angle of 74° [46]. The ACE-FTS covers the 750–4400 cm $^{-1}$ range with a high spectral resolution of 0.02 cm^{-1}. It provides vertical profiles of trace gas VMRs and temperature across latitudes from 85° S to 85°N. The vertical resolution is approximately 4 km from the cloud tops up to about 150 km [47].

The retrieval of ACE-FTS CH_4 products from atmospheric spectra involves two steps. The first step is deriving the pressure and temperature profiles using the spectral lines of carbon dioxide. Second, CH_4 VMR profiles are retrieved using a modified global fitting approach, in which all parameters are determined with the LM nonlinear least-squares method [48]. The retrieval product is not sensitive to the initial profiles and does not include averaging kernels. The uncertainties reported in the data files are the statistical fitting errors resulting from the least-squares process and do not account for systematic components or parameter correlations [48], [49].

The HITRAN 2016 spectroscopic line parameters and the Voigt line shape were used in the ACE-FTS V4.1 retrieval calculations, employing a similar methodology to that used for AIUS retrievals. More detailed explanations of the retrieval algorithms can be found in [48], [50], and [51].

The accuracy of the version v2.2 CH_4 data is within 10% from the upper troposphere to the lower stratosphere, and within 25% in the middle and higher stratosphere up to the lower mesosphere (<60 km) when compared with correlative satellite, balloon-borne, and ground-based data [10]. In Version 4 (with version 4.1), which represents the most recent update, the retrieval utilizes the latest spectroscopic information and features improved accuracy in forward model calculations [51]. In this article, we compared ACE-FTS CH_4 data V4.1 with AIUS data. The data are available online.[2]

For the comparison experiment, we limited the spatial coincidence to within 1.5° (approximately 150 km) and the temporal coincidence to within 36 h between AIUS and ACE-FTS. As a

[2][Online]. Available: https://databace.scisat.ca/level2/ace_v4.1_v4.2/

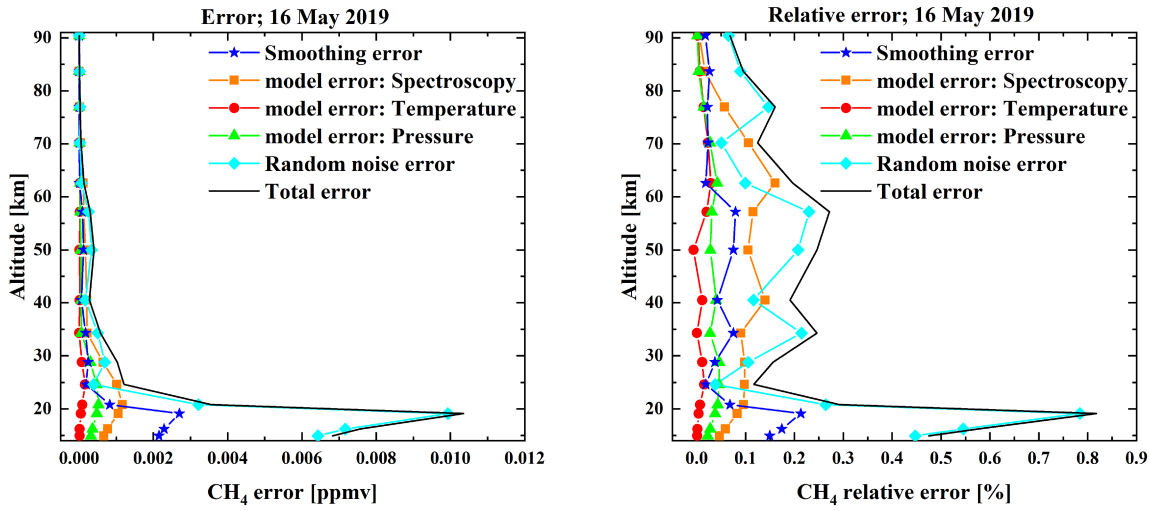

Fig. 10. Individual estimates of smoothing, forward model, and noise errors for CH_4 retrieval. The absolute and relative errors correspond to the retrieval was carried for AIUS measurements recorded on May 16, 2019. Assumed uncertainties in the forward model errors are given in Table IV. The solid black line (Total error) represents the root sum squares of the smoothing error, forward model error, and random noise error.

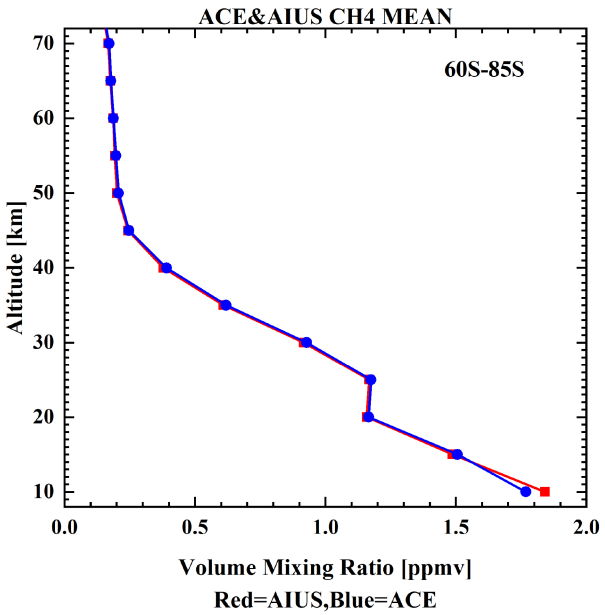

Fig. 11. Mean AIUS (red line) and ACE-FTS (blue line) profiles of the 42 matching pairs in the 60–85°S latitude zone are included in the comparison.

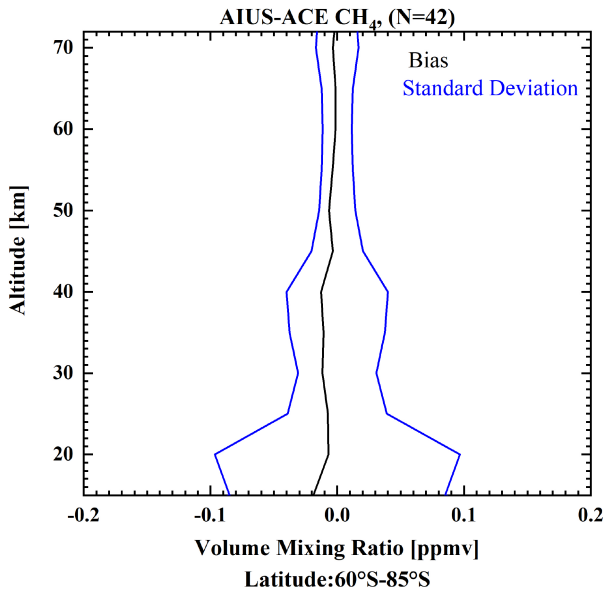

Fig. 12. Difference between AIUS and ACE-FTS profiles of CH_4.

result, we obtained 42 orbits of AIUS data that met the matching criteria.

The range of altitude in which both instruments have good sensitivity is limited by the AIUS data at the lower boundary and by the ACE-FTS data at the upper boundary. We have set the lower altitude at 10 km and the upper altitude at 70 km. The inversion errors in this altitude range are very low, resulting in an uncertainty of 2–3% for ACE-FTS CH_4, while it may be more than 10% at the lowest and highest altitudes of the retrieval [10].

We needed to consider the difference in vertical resolution between the AIUS and the ACE-FTS when comparing their CH_4 products. Indeed, the AIUS has a vertical resolution of approximately 4–11 km (with an altitude range of 10–60 km), whereas ACE-FTS has a resolution of around 4 km. In order to facilitate comparison, the AIUS and ACE-FTS data are interpolated into a unified grid with intervals of 10, 15, 20, 25, 30, 35, 40, 45, 50, 55, 60, 65, and 70 km. The comparisons between AIUS and ACE-FTS CH_4 profiles are shown in Figs. 11–13.

Fig. 11 shows the mean CH_4 profiles of the AIUS and ACE-FTS between 10 and 70 km. It indicates that the AIUS and ACE-FTS CH_4 mean profiles are in good agreement. The CH_4 concentrations retrieved by the AIUS are slightly higher than those retrieved by ACE-FTS at 10 km.

The quantitative differences between AIUS and ACE-FTS are illustrated in Figs. 12 and 13. These differences are presented in absolute units and as percentages relative to ACE-FTS, respectively. The average relative standard deviation of the differences is smaller than 7.2% below 70 km.

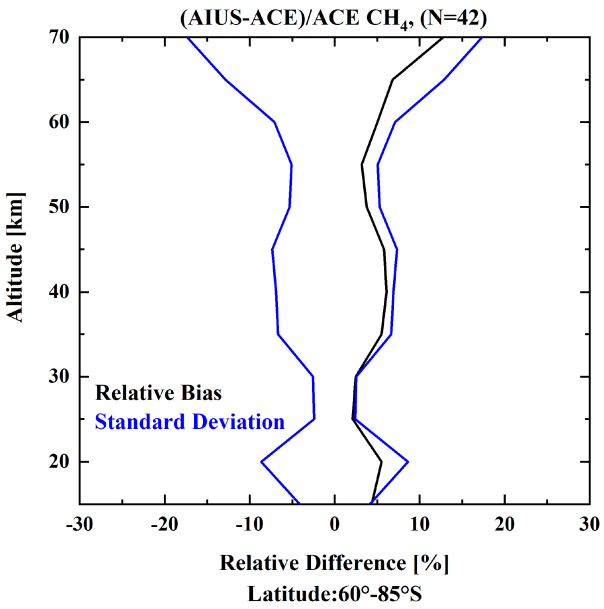

Fig. 13. Percentage relative difference between AIUS and ACE-FTS profiles of CH_4.

IV. Conclusion

This article provides the CH_4 retrievals and an assessment of the atmospheric CH_4 profiles obtained during the second year of the AIUS mission, in order to quantify the level of agreement with other available instruments. The AIUS CH_4 products are retrieved from solar occultation measurements, using 120 spectral bands located between 1203 and 2906 cm^{-1}.

The inversion results indicate that CH_4 mole fractions show significant variations in latitude and season over Antarctica. The CH_4 VMR is approximately 1.17–1.65 ppmv between 10 and 20 km, and decreases to less than 0.2 ppmv at 35 km in April and May.

The results of the error analysis indicate that the majority of the total error is caused by spectroscopic, random noise and smoothing errors. The uncertainties in temperature and pressure have a relatively minor impact on the total error. The comparison between AIUS CH_4 profiles and ACE-FTS CH_4 profiles reveals that the average relative standard deviation of the differences is smaller than 7.2% below 70 km.

In future work, the retrieval algorithm will be improved to retrieve more trace gases, such as HCN, CCl_4, SF_6, etc. Comparisons with ACE-FTS, ground stations, and other datasets are required for further validation.

Acknowledgment

The AIUS, ACE-FTS, and MLS data used in this study were acquired from the China Center for Resources Satellite Data and Application[3], ACE/SCISAT Database[4], and EARTHDATA[5], respectively. The authors would like to thank the Global Monitoring Laboratory for providing the trends in CH_4, and the HITRAN group members for providing the HITRAN online data.

[3][Online]. Available: https://data.cresda.cn/
[4][Online]. Available: https://databace.scisat.ca/
[5][Online]. Available: https://disc.gsfc.nasa.gov/

References

[1] M. Zhou et al., "Atmospheric CO and CH_4 time series and seasonal variations on Reunion island from ground-based in situ and FTIR (NDACC and TCCON) measurements," *Atmospheric Chem. Phys.*, vol. 18, no. 19, pp. 13881–13901, 2018.
[2] S. Kirschke et al., "Three decades of global methane sources and sinks," *Nature Geosci.*, vol. 6, no. 10, pp. 813–823, Oct. 2013.
[3] D. Blake, E. Mayer, S. Tyler, Y. Makide, D. Montague, and F. Rowland, "Global increase in atmospheric methane concentrations between 1978 and 1980," *Geophys. Res. Lett.*, vol. 9, no. 4, pp. 477–480, 1982.
[4] X. Lan, K. Thoning, and E. Dlugokencky, "Trends in globally-averaged CH_4, N_2O, and SF_6 determined from NOAA global monitoring laboratory measurements. version 2023-06," 2023, doi: 10.15138/P8XG-AA10.
[5] R. Jones and J. Pyle, "Observations of CH_4 and N_2O by the NIMBUS -7 SAMS—A comparison with in situ data and two-dimensional numerical-model calculations," *J. Geophys. Res.-Atmos.*, vol. 89, no. ND4, pp. 5263–5279, 1984.
[6] S. Noel et al., "Stratospheric CH_4 and CO_2 profiles derived from SCIAMACHY solar occultation measurements," *Atmos. Meas. Techn.*, vol. 9, no. 4, pp. 1485–1503, 2016.
[7] O. Schneising et al., "A scientific algorithm to simultaneously retrieve carbon monoxide and methane from TROPOMI onboard SENTINEL-5 precursor," *Atmospheric Meas. Techn.*, vol. 12, no. 12, pp. 6771–6802, 2019. [Online]. Available: https://amt.copernicus.org/articles/12/6771/2019/
[8] T. von Clarmann et al., "Retrieval of temperature, H2O, O3, HNO3, CH_4, N_2O, ClONO2 and ClO from MIPAS reduced resolution nominal mode limb emission measurements," *Atmos. Meas. Techn.*, vol. 2, no. 1, pp. 159–175, 2009.
[9] X. Xiong et al., "Characterization and validation of methane products from the atmospheric infrared sounder (AIRS)," *J. Geophys. Res.-Biogeosci.*, vol. 113, Jul. 2008.
[10] M. De Maziere et al., "Validation of ACE-FTS V2.2 methane profiles from the upper troposphere to the lower mesosphere," *Atmospheric Chem. Phys.*, vol. 8, no. 9, pp. 2421–2435, 2008.
[11] R. Beer, T. Glavich, and D. Rider, "Tropospheric emission spectrometer for the Earth observing system's aura satellite," *Appl. Opt.*, vol. 40, no. 15, pp. 2356–2367, May 2001.
[12] T. Tanaka et al., "Characterization and validation of CO_2 and CH_4 products derived from the GOSAT thermal infrared band," *Proc. SPIE*, vol. 8528, pp. 175–178, 2012.
[13] A. de lange and J. Landgraf, "Methane profiles from GOSAT thermal infrared spectra," *Atmos. Meas. Techn.*, vol. 11, no. 6, pp. 3815–3828, Jun. 2018.
[14] Y. Sun et al., "Hyper-spectral observation satellite and it's application prospects," *Aerosp. Shanghai*, vol. 34, no. 3, pp. 1–13, 2017.
[15] Q. Tao et al., "Long life assurance technology of GF-5 satellite," *Aerosp. Shanghai*, vol. 36, no. S2, pp. 18–23, 2019.
[16] X. Li et al., "Monitoring trace gases over the Antarctic using atmospheric infrared ultraspectral sounder onboard GaoFen-5: Algorithm description and first retrieval results of O_3, H_2O, and HCL," *Remote Sens.*, vol. 11, no. 17, 2019, Art. no. 1991.
[17] C. Liangfu et al., "Mission overview of the GF-5 satellite for atmospheric parameter monitoring," *Nat. Remote Sens. Bull.*, vol. 25, no. 9, pp. 1917–1931, 2021.
[18] H. Wang et al., "Assessment of retrieved N_2O, NO_2, and HF profiles from the atmospheric infrared ultraspectral sounder based on simulated spectra," *Sensors*, vol. 18, no. 7, 2018, Art. no. 2209.
[19] X. F. Cao and X. Y. Li, "Channel selection for AIUS temperature inversion based on GF-5," (in Chinese), *J. Remote Sens.*, vol. 24, no. 10, pp. 1157–1167, 2020.
[20] X. Cao, X. Li, S. Liu, and X. Zhang, "Assessment of spectra of the atmospheric infrared ultraspectral sounder on GF-5 and validation of water vapor retrieval," *Sensors*, vol. 21, no. 2, 2021.
[21] L. Loulergue et al., "Orbital and millennial-scale features of atmospheric CH_4 over the past 800,000 years," *Nature*, vol. 453, no. 7193, pp. 383–386, 2008.
[22] J. Jouzel et al., "Extending the Vostok ice-core record of paleoclimate to the penultimate glacial period," *Nature*, vol. 364, no. 6436, pp. 407–412, 1993.

[23] L. L. Du, L. Liu, S. L. Ge, Z. W. Li, C. J. Zhou, and G. S. Ding, "High precision on-orbit spectral calibration of atmospheric infrared ultra-spectral sounder," *J. Infrared Millimeter Waves*, vol. 40, no. 2, pp. 214–222, 2021.
[24] L. Hou, P. Xu, Y. Zhang, and L. Li, "Key technologies of atmospheric infrared ultra-resolution spectrometer," *Aerosp. Shanghai*, vol. 36, no. S2, pp. 117–125, 2019.
[25] J. Xu, "Inversion for limb infrared atmospheric sounding," Doctoral dissertation, Technische Universität München, Munich, Germany, 2016.
[26] K. N. Liou, *An Introduction to Atmospheric Radiation*, Dept. Atmos. Sci., Univ. California, Los Angeles, Los Angeles, California, Elsevier, vol. 84, pp. 1–583, 2002.
[27] A. Dudhia, "The reference forward model (RFM)," *J. Quantitative Spectrosc. Radiative Transfer*, vol. 186, pp. 243–253, 2017.
[28] T. von Clarmann et al., "Intercomparison of radiative transfer codes under non-local thermodynamic equilibrium conditions," *J. Geophys. Res.-Atmos.*, vol. 107, no. D22, pp. ACH-12, 2002.
[29] C. D. Rodgers, *Series Atmos., Ocean. Planet. Phys.: Volume 2 Inverse Methods Atmos. Sounding Theory Pract.*, p. 256, Jul. 2000, doi: 10.1142/3171.
[30] C. D. Rodgers, "Retrieval of atmospheric-temperature and composition from remote measurements of thermal-radiation," *Rev. Geophys.*, vol. 14, no. 4, pp. 609–624, 1976.
[31] J. Xu et al., "Performance assessment of balloon-borne trace gas sounding with the terahertz channel of telis," *Remote Sens.*, vol. 10, no. 2, 2018.
[32] J. Xu, F. Schreier, A. Doicu, and T. Trautmann, "Assessment of Tikhonov-type regularization methods for solving atmospheric inverse problems," *J. Quantitative Spectrosc. Radiative Transfer*, vol. 184, pp. 274–286, 2016.
[33] J. Xu, L. Rao, F. Schreier, D. S. Efremenko, A. Doicu, and T. Trautmann, "Insight into construction of Tikhonov-type regularization for atmospheric retrievals," *Atmosphere*, vol. 11, no. 10, 2020, Art. no. 1052.
[34] I. E. Gordon et al., "The HITRAN2016 molecular spectroscopic database," *J. Quantitative Spectrosc. Radiative Transfer*, vol. 203, pp. 3–69, 2017.
[35] G. Echle et al., "Optimized spectral microwindows for data analysis of the Michelson interferometer for passive atmospheric sounding on the environmental satellite," *Appl. Opt.*, vol. 39, no. 30, pp. 5531–5540, 2000.
[36] S. Zhang, "Hyperspectral atmospheric sounding information channel selection study," *J. Meteorological Sci.*, vol. 29, no. 4, pp. 4475–4481, 2009.
[37] M. N. Deeter et al., "Operational carbon monoxide retrieval algorithm and selected results for the MOPITT instrument," *J. Geophys. Res., Atmospheres*, vol. 108, no. D14, 2003.
[38] M. Maslin, M. Owen, R. Betts, S. Day, T. D. Jones, and A. Ridgwell, "Gas hydrates: Past and future geohazard?," *Philos. Trans. Roy. Soc. A, Math. Phys. Eng. Sci.*, vol. 368, no. 1919, pp. 2369–2393, 2010.
[39] M. J. Schwartz et al., "Validation of the aura microwave limb sounder temperature and geopotential height measurements," *J. Geophys. Res., Atmospheres*, vol. 113, no. D15, 2008. [Online]. Available: http://000255594400001
[40] N. J. Livesey et al., "Earth observing system (EOS) aura microwave limb sounder (MLS) version 4.2x level 2 and 3 data quality and description document," Tech. Rep., 2020. [Online]. Available: https://mls.jpl.nasa.gov/data/v4-2_data_quality_document.pdf
[41] E. F. Fishbein et al., "Validation of UARS microwave limb sounder temperature and pressure measurements," *J. Geophys. Res., Atmospheres*, vol. 101, no. D6, pp. 9983–10016, 1996. [Online]. Available: http://WOS:A1996UJ40400022
[42] Y. A. Ba et al., "MeCaSDa and ECaSDa: Methane and ethene calculated spectroscopic databases for the virtual atomic and molecular data centre," *J. Quantitative Spectrosc. Radiative Transfer*, vol. 130, pp. 62–68, 2013. [Online]. Available: http://WOS:000326482100004
[43] L. R. Brown et al., "Methane line parameters in the HITRAN2012 database," *J. Quantitative Spectrosc. Radiative Transfer*, vol. 130, pp. 201–219, 2013. [Online]. Available: http://WOS:000326482100015
[44] L. R. Brown et al., "Methane line parameters in HITRAN," *J. Quantitative Spectrosc. Radiative Transfer*, vol. 82, no. 1-4, pp. 219–238, 2003. [Online]. Available: http://WOS:000184738800011
[45] J. Loos, M. Birk, and G. Wagner, "Measurement of air-broadening line shape parameters and temperature dependence parameters of H_2O lines in the spectral ranges 1850–2280 cm(-1) and 2390–4000 cm (-1)," *J. Quantitative Spectrosc. Radiative Transfer*, vol. 203, pp. 103–118, 2017. [Online]. Available: http://WOS:000414107400005
[46] F. Hase, L. Wallace, S. D. McLeod, J. J. Harrison, and P. F. Bernath, "The ACE-FTS Atlas of the infrared solar spectrum," *J. Quantitative Spectrosc. Radiative Transfer*, vol. 111, no. 4, pp. 521–528, 2010.
[47] P. F. Bernath et al., "Atmospheric chemistry experiment (ACE): Mission overview," *Geophys. Res. Lett.*, vol. 32, no. 15, 2005.
[48] C. D. Boone et al., "Retrievals for the atmospheric chemistry experiment Fourier-transform spectrometer," *Appl. Opt.*, vol. 44, no. 33, pp. 7218–7231, 2005.
[49] E. Dupuy et al., "Validation of ozone measurements from the atmospheric chemistry experiment (ACE)," *Atmospheric Chem. Phys.*, vol. 9, no. 2, pp. 287–343, 2009.
[50] C. D. Boone, K. A. Walker, and P. F. Bernath, "Version 3 retrievals for the atmospheric chemistry experiment Fourier transform spectrometer (ACE-FTS)," in *The Atmospheric Chemistry Experiment ACE at 10: A Solar Occultation Anthology*. 2013, pp. 103–27.
[51] C. D. Boone, P. F. Bernath, D. Cok, S. C. Jones, and J. Steffen, "Version 4 retrievals for the atmospheric chemistry experiment Fourier transform spectrometer (ACE-FTS) and imagers," *J. Quantitative Spectrosc. Radiative Transfer*, vol. 247, 2020, Art. no. 106939.

Shuanghui Liu received the B.E. degree in remote sensing science and technology from the Shandong University of Science and Technology, Qingdao, China, in 2019, and the M.E. degree in electronic and communication engineering from the University of Chinese Academy of Sciences, Beijing, China, in 2022. In 2022, she joined the National Space Science Center, Chinese Academy of Sciences, Beijing, China.

Her research interests include atmospheric composition inversion and quantitative remote sensing applications.

Xiaoying Li received the B.S. degree in geography from Fujian Normal University, Fuzhou, China, in 1999, and the M.S. degree in geography from Beijing Normal University, Beijing, China, in 2002, and the Ph.D. degree in quantitative remote sensing from the Institute of Remote Sensing Applications, Chinese Academy of Sciences, Beijing, in 2006.

She is working as an Associate Research Fellow with the Aerospace Information Research Institute, Chinese Academy of Sciences. Her research interests include research on atmospheric composition inversion algorithms and quantitative algorithms for optical image remote sensing information.

Jian Xu (Senior Member, IEEE) received the B.E. degree in geographic information systems from Hohai University, Nanjing, China, in 2004, and the M.S. degree in Earth-oriented space science and technology and the Ph.D. degree in atmospheric remote sensing from Technische Universität München, Münich, Germany, in 2009 and 2015, respectively.

From 2010 to 2021, he was with the Remote Sensing Technology Institute (IMF), German Aerospace Center (DLR), Oberpfaffenhofen, Germany. He was involved in the development/refinement of atmospheric retrieval algorithms for ESA's Sentinel-5P and Sentinel-4 satellite missions. He is currently a Professor with the National Space Science Center, Chinese Academy of Sciences, Beijing, China. His research interests include remote sensing of planetary atmosphere, radiative transfer modeling, and ill-posed inverse problems.

Hailiang Shi received the B.S. degree in surveying and mapping engineering from the Xi'an University of Science and Technology, Xi'an, China, in 2004, and the Ph.D. degree in optics from the Chinese Academy of Sciences (CAS), Hefei, China, in 2012.

He is the Principle Investigator of the Greenhouse Gas Monitoring Instrument (GMI) data processing and has developed the ground data processing system for this payload with the CAS. His main research interests include hyperspectral atmospheric remote sensing, instrument calibration, and data characterization.

Yuhang Guo received the B.E. degree in geographic information science from the Taiyuan University of Technology, Taiyuan, China, in 2021. He is currently working toward the M.E. degree in resources and environment from the University of Chinese Academy of Sciences, Beijing, China.

His research interests include atmospheric composition inversion and optimal estimation methods researches.

Xingying Zhang received the B.S. degree in material science and engineering from the Beijing University of Aeronautics and Astronautics, Beijing, China, in 2001, and the Ph.D. degree in atmospheric chemistry from Beijing Normal University, Beijing, in 2006.

He is currently the Deputy Director of Technology and Climate Change, China Meteorological Administration, Beijing. He has authored and co-authored more than 80 research articles in science journals and books. His research interests include satellite observation and in situ measurement of atmospheric components and its applications to climate and environmental problems.

Shule Ge received the B.S. degree in electronic science and technology and the Ph.D. degree in optical engineering from the Beijing Institute of Technology, Beijing, China, in 2005 and 2010, respectively.

He is currently a Researcher with the China Center for Resources Satellite Data and Application, Beijing. His research interests include processing and calibration of hyperspectral and multispectral remote sensing data, atmospheric LiDAR data processing, and hyperspectral image classification.

Yapeng Wang received the master's degree in electronics and communication engineering and the Ph.D. degree in cartography and geographic information systems from the Institute of Remote Sensing and Digital Earth, Chinese Academy of Sciences, Beijing, China, in 2017 and 2020, respectively.

She joined the National Satellite Meteorological Center (National Center for Space Weather), Beijing, as a Research Assistant, in 2020. Since 2020, she has been participating in the ground data processing system construction of the FengYun satellite project and responsible for the algorithm research of ozone products based on hyperspectral infrared atmospheric sounder (HIRAS) and geostationary interferometric infrared sounder (GIIRS). Her research interests include atmospheric components retrieval from hyperspectral satellite data, mainly involved in the development of ozone precursors and ozone profiles retrieval algorithms.

Hongmei Wang received the master's degree in cartography and geographic information engineering from the Kunming University of Science and Technology, Kunming, China, in 2015, and the Ph.D. degree in cartography and geographic information systems from the Institute of Remote Sensing and Digital Earth, Chinese Academy of Sciences, Beijing, China, in 2019.

In 2019, she joined Nantong University, Nantong, China. Since 2012, she has been a Researcher in remote sensing. Her research interests include remote sensing application, ultraviolet limb, infrared occultation, and terahertz limb atmospheric composition inversion.

Xifeng Cao received the B.E. degree in remote sensing science and technology from the Shandong University of Science and Technology, Qingdao, China, in 2018, and the M.E. degree in electronic and communication engineering from the University of Chinese Academy of Sciences, Beijing, China, in 2021. In 2021, she joined China Meteorological Administration, Beijing.

Her research interests include carbon dioxide inversion based on LiDAR.

Lanlan Rao received the master's degree in cartography and geographic information engineering from the China University of Mining and Technology, Xuzhou, China, in 2017, and the Ph.D. degree in atmospheric remote sensing from the German Aerospace Center (DLR), Remote Sensing Technology Institute (IMF), Weßling, Germany, and the Technical University of Munich (TUM), Munich, Germany, in 2022.

Her research interests include remote sensing of aerosol properties from satellite data.

Jiancheng Shi (Fellow, IEEE) received the M.S. degree and the Ph.D. degree in school of computational earth systems science from the University of California, Santa Barbara, USA, in 1987 and 1991, respectively.

He is currently a Senior Research Scientist with the National Space Science Center, Chinese Academy of Sciences, Beijing, China. He has authored and co-authored more than 500 papers with nearly 14 000 citations. His research interests mainly include remote sensing theory and techniques; remote sensing of cryosphere components, water cycle components, and radiation energy balance; development of new satellite missions; and synergy of remote sensing observations and Earth process models for hydrology and climatic change.

Dr. Shi is the Fellow of the SPIE.